Journal of Materials Chemistry A

ROYAL SOCIETY OF CHEMISTRY

PAPER

View Article Online
View Journal | View Issue

Cite this: J. Mater. Chem. A, 2025, 13, 41215

From volcanic ashes to magnetic zeolites: unravelling the iron oxide phase transitions by magnetic and advanced structural characterization

Maryam Abdolrahimi, [ab] Pierfrancesco Maltoni, [ab] Gianni Barucca, [c] Claudia Belviso,[d] Carlo Meneghini [e] and Davide Peddis *[ab]

Received 30th April 2025
Accepted 23rd October 2025

DOI: 10.1039/d5ta03456f

rsc.li/materials-a

Volcanic ashes, rich in iron-containing phases, present an underexplored resource for creating functional materials. In this study, we investigate the hydrothermal transformation of volcanic ashes from Mount Etna (Sicily, Italy) into magnetic zeolites, exploring both structural and magnetic evolution. By combining X-ray absorption spectroscopy (Fe K-edge) and magnetometry, we reveal how the phase transition from olivine to magnetite-like phases, and hematite influences the magnetic behaviour. We observe distinct changes in iron oxidation states, coordination, and the emergence of antiferromagnetic contributions. This work highlights the potential of volcanic ashes as a sustainable source for designing advanced materials with tunable magnetic properties.

1. Introduction

Magnetic minerals are ubiquitous in different regions of the Earth, especially in rocks and sediments,[1] and many of the magnetic components are present in the form of nanoparticles.[2] There are lots of volcanoes on the Earth producing different sources of magnetic nanoparticles (MNPs), ranging from obsidian[3] to volcanic ashes,[4] which contain amorphous silica and crystalline quartz, respectively. The most important magnetic carriers in rocks and soils are iron oxides, iron–titanium oxides, and iron oxyhydroxides.[5] Magnetite (Fe_3O_4), maghemite (γ-Fe_2O_3) and related ferrimagnetic materials, such as titanomagnetite, are the materials with the largest saturation magnetization. Hematite (α-Fe_2O_3) and other antiferromagnetic materials, such as olivine $(Mg,Fe)_2SiO_4$, ilmenite ($FeTiO_3$) and goethite (α-FeOOH), have a much smaller net magnetization per unit mass. However, hematite can be a significant carrier of remanent magnetization when it is in a nanoscale lamellar structure with ilmenite.[6] The presence of iron oxides/hydroxides in the chemical composition of natural resources makes these materials suitable for designing novel materials with tailored properties.

In the pursuit of sustainable and recyclable materials, researchers have focused on hybrid structures that combine the benefits of natural minerals with functional nanomaterials. Among these, magnetic zeolites[7] have attracted significant attention, as they merge the exceptional adsorption properties of zeolites with the magnetic behaviour of iron oxides. This unique combination makes them highly versatile for a wide range of applications, from catalysis to polluted water remediation.[8–12]

Several studies have explored the magnetic behaviour of natural resources,[13] such as rhyolitic glasses, volcanic ashes and clays. However, understanding the magnetic behaviour of such materials using macroscopic techniques remains an open challenge, because of the variety of magnetic phases in natural resources, and the possible high dilution of such phases in non-magnetic ones.[14] Typically, X-ray absorption fine structure (XAFS)[15–17] and Mössbauer spectroscopy[18–20] techniques were used to make qualitative considerations; however, to the best of our knowledge, no quantitative analysis has been conducted to study the possible phase transitions and oxidation state of Fe when they are converted from natural resources to magnetic zeolites.

In our previous study, we demonstrated that volcanic ashes from Mt. Etna can serve as a promising precursor for synthesizing magnetic zeolites, owing to the presence of nanostructured iron oxide/hydroxide phases.[4] The transformation of volcanic ashes into zeolitic materials offers a sustainable and cost-effective approach for producing functional materials with applications in energy and environmental fields. Zeolites, with their high surface area, tunable porosity, and ion-exchange

[a]Institute of Structure of Matter, nM2-Lab, National Research Council, Monterotondo Scalo, Rome, 00015, Italy
[b]Department of Chemistry and Industrial Chemistry & INSTM RU, nM2-Lab, University of Genoa, Genoa 16146, Italy. E-mail: davide.peddis@unige.it
[c]Department of Science and Engineering of Matter, Environment and Urban Planning (SIMAU), University Politecnica Delle Marche, Via Brecce Bianche 12, Ancona 60131, Italy
[d]Istituto di Metodologie per L'Analisi Ambientale IMAA–CNR, Tito Scalo, Potenza, 85050, Italy
[e]Department of Sciences, University of Roma Tre, Via Della Vasca Navale 84, Rome 00146, Italy

capacity, are widely used in catalysis, gas separation, and CO_2 capture.[21,22] More recently, their potential has extended to applications like hydrogen generation, photocatalysis, and sensors.[23,24] By converting volcanic ash, particularly rich in silicate and olivine phases, into magnetic zeolites, containing magnetite-like phases, our work presents a method that not only provides high yields but also adds magnetic properties that can enhance their performance in various applications.[25,26] This approach contributes to the development of green materials by recycling waste products and offers a pathway for sustainable material synthesis.

In this work, we shed some light on the zeolitization process by a detailed investigation of the magnetic and atomic structure of both the pristine volcanic ash and the zeolites derived from it. In this process, both the magnetic phase and the zeolitic framework form *in situ*, without any external addition of magnetic nanoparticles. This approach leads to a unique class of materials, where the magnetic and zeolitic components co-evolve from the same precursor under hydrothermal conditions. We focus primarily on the structural and magnetic characterization of zeolitized volcanic ash-based materials, while detailed application testing—particularly related to water treatment—is not repeated here but has been experimentally validated in our previous work.[4] Given the complex nature of magnetic phases in natural resources, a chemically sensitive probe of iron species is essential for an accurate assessment of their magnetic properties. To this end, Fe K-edge X-ray Absorption Spectroscopy (XAS) was employed to determine the Fe valence state and coordination chemistry, providing critical insights into the role of iron in structural and magnetic transformations.

The X-ray absorption near-edge structure (XANES) region of the XAS spectra provides information about the average electronic structure of the absorbing atoms (oxidation states, vacant orbitals, and electronic configuration) and their chemical speciation (site symmetry and coordination chemistry).[27] In the specific case of Fe oxides, the analysis of pre-edge regions of the XANES spectra has been used to precisely evaluate the average Fe valence state and coordination number.[28] In volcanic ashes, Fe cations may reside in several crystalline phases such as magnetite, maghemite, hematite, ilmenite and olivine as well as in amorphous/highly disordered phases which cannot be proved by standard XRD methods. Considering the complex matrix within which Fe cations assume different oxidation states depending on the phases, XAFS serves as a powerful technique for selectively probing the average local coordination environment and oxidation state of iron, enabling a deeper understanding of the correlation between structural transformations and magnetic behaviour.[29]

2. Experimental

2.1. Sample preparation

Volcanic ashes, the result of an eruption during the volcanic activity of Etna, were collected from three different regions around the volcano: from the upper part of Etna (named VA0),

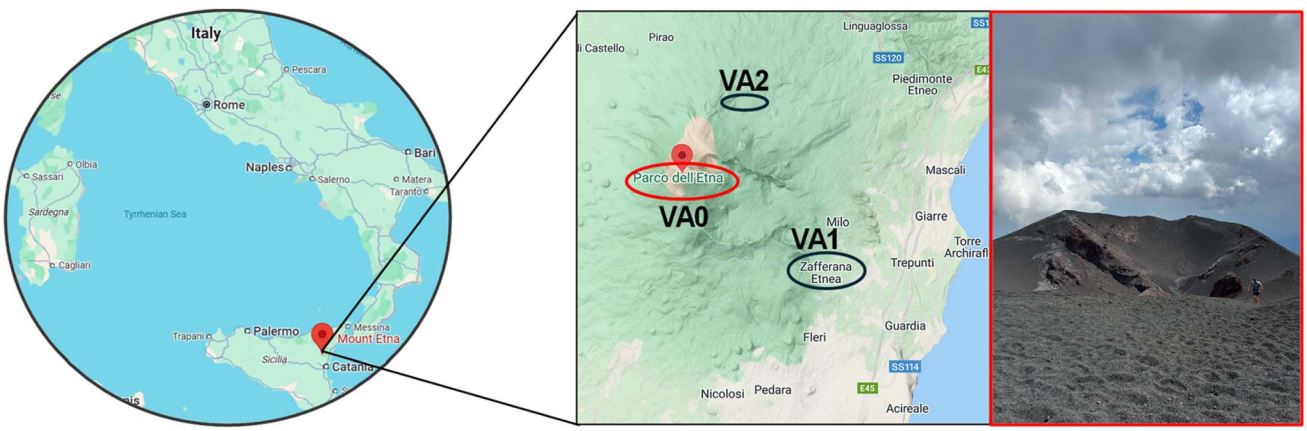

Fig. 1 Map showing the location and different sites of the Etna volcano where the raw VA samples were collected.

Table 1 VA sample labels and characteristic features

Volcanic ashes		Synthesised magnetic zeolites	
Label	Characteristic features	Label	Solution
VA1	Weathering and anthropic pollution	$VA1H_{60}$	Distilled water
		$VA1HM_{60}$	Seawater
VA2	Weathering pollution	$VA2H_{60}$	Distilled water
		$VA2HM_{60}$	Seawater
VA0	Near crater ashes (no impact from pollution)	$VA0H_{60}$	Distilled water
		$VA0HM_{60}$	Seawater

a nearby town located on the slope of the mountain, Zafferana Etnea (at 74 m height above sea level) (named VA1), and the area surrounding Chalet Sapienza, 2500 m height above sea level (named VA2) (Fig. 1). Regarding the chosen regions, VA1 was influenced by both weathering and anthropic pollution, while VA2 was only affected by weathering pollution. According to the European Waste Catalogue (EWC),[30] both VA1 and VA2 are classified as municipal waste residues (*code 20-03-03*). In contrast, VA0 was not impacted by either weathering or anthropic activities.

The synthesis of zeolites was performed with the collected powders at 60 °C using both distilled water (H) and sea water (HM) following the procedure described in the previous paper of co-authors.[4] We refer to those samples as $VAXH_{60}$ and $VAXHM_{60}$, where X stands for the sample (0, 1 and 2), respectively, and 60 indicates the temperature of incubation. All chemicals were purchased from Sigma-Aldrich. Labels for the samples are reported in Table 1.

2.2. Characterization techniques

The structural and morphological analyses of the raw materials and synthetic products were performed by X-ray diffraction (XRD), and scanning (SEM) and transmission (TEM) electron microscopy, respectively. Details of the XRD and SEM instruments and measurement conditions are reported in the previous paper.[4] Briefly, XRD patterns were collected in θ–2θ geometry over the angular range of 3–70°, using Cu Kα radiation ($\lambda = 1.5406$ Å), with a step size of 0.02° and a scan time of 3s per step. Cu Kα has been chosen in line with previous studies.[4] TEM analysis was performed using a Philips CM200 microscope operating at 200 kV. For TEM observations, samples in the form of powder were dispersed in ethanol. A drop of the suspension was deposited on a commercial holey-carbon grid for TEM, and held in air until ethanol evaporation.

The magnetic properties were studied using a Quantum Design SQUID magnetometer ($H_{max} = \pm 5$ T, $T = 5$–300 K) as well as a vibrating sample magnetometer (VSM Model 10 – Microsense) equipped with an electromagnet ($\mu_0 H_{max} = \pm 2$ T, $T = 300$ K). Zero field cooled–field cooled (ZFC–FC) protocols were used to record the magnetization *versus* temperature within 5–300 K under an applied field of 2.5 mT. The ZFC magnetic curve was obtained by heating the sample from 5 K to 300 K under a magnetic field, after a cooling process in a zero magnetic field. The FC magnetic curve was obtained by cooling the sample from 300 K to 5 K under the applied magnetic field. The field dependence of the magnetization has also been studied at both low temperature (5 K) and room temperature (300 K). The powders were fixed using epoxy resin in polycarbonate capsules to prevent any movement of the sample during the measurement. All the magnetic data are normalized by the total mass of the magnetic phase (~12%) of the samples. The magnetic fraction was estimated under the assumption that all iron detected in the composite is present as ferrimagnetic iron oxides (*e.g.*, Fe_3O_4 or γ-Fe_2O_3), based on the synthesis conditions and observed magnetic behavior. Total Fe content was quantified by inductively coupled plasma optical emission spectroscopy (ICP-OES), and the corresponding mass percentage of the magnetic phase was calculated accordingly. Specifically, the Fe(III) concentration obtained from ICP-OES was converted to iron oxide by applying a stoichiometric factor, based on the molar mass ratio between iron oxide and elemental Fe(III). In practice, the concentration was first obtained as elemental Fe(III), and then converted to Fe_2O_3 by applying the factor $Fe_2O_3\% = Fe\ (wt\%) \times M_{Fe2O3}/(2 \times M_{Fe}) = Fe\ (wt\%) \times 159.69/(2 \times 55.845) \approx Fe\ (wt\%) \times 1$. This procedure yielded Fe_2O_3 contents reported in Table 2. To estimate the fraction of magnetic phases, we assumed that the Fe_2O_3 originates entirely from iron oxides, including both magnetic (Fe_3O_4 and γ-Fe_2O_3) and antiferromagnetic (α-Fe_2O_3) phases. This method provides an upper-limit for estimation of the magnetic component within the sample.

Table 2 Results of ICP analysis of the volcanic ash samples

	Conc final (%)			SD (%)		
	VA0	VA1	VA2	VA0	VA1	VA2
Al_2O_3	16.4	16.9	13.2	0.2	0.1	0.1
CaO	10.5	10.7	11.6	0.1	0.1	0.1
Fe_2O_3	11.4	10.9	13.3	0.1	0.1	0.1
MgO	6.4	5.3	10.4	0.2	0.1	0.2
Na_2O	3.5	3.2	2.4	0.1	0.1	0.1
SiO_2	44.5	46.6	43.8	0.3	0.2	0.1

The Fe K-edge XAS measurements were performed at the XAFS beamline (Exp. #20195485) of the ELETTRA synchrotron facility (Trieste, Italy).[31] The XAFS beamline exploits the synchrotron radiation emitted by the 11.1 ELETTRA bending magnet. The synchrotron X-ray beam is first vertically reflected using a collimating Pt-coated Si mirror ensuring efficacious harmonic rejection, and the beam energy was tuned using a double Si(111) crystal monochromator. The sample powders were ground, mixed with the polyvinylpyrrolidone (PVP) polymer in approximately 1/10 weight concentration and pressed (at 5 kbar) to obtain thin solid pellets (13 mm diameter). The Fe K-edge ($E_{Fe} = 7112$ eV) XAS measurements were carried out in transmission mode at room temperature in the 7100 eV to 7250 eV energy range in the near-edge region (XANES). The edge jump discontinuities were in the range of 0.2–0.8 for all the samples. Incident (I_o) and transmitted (I_t) intensities were measured using two gas filled ionization chambers. Fe foil was placed after the I_t chamber, and the transmitted X-ray intensity was measured using a third ionization chamber (I_r). The sample and Fe reference absorption signals ($\alpha = \mu t$) were calculated as $\alpha(E) = \ln(I_o/I_t)$ and $\alpha_r(E) = \ln(I_t/I_r)$, respectively.[32] Three scans were collected for each sample and averaged (after checking for the correct energy scale) to improve the data statistics and avoid artefacts due to X-ray beam drifts or instabilities. The raw $\alpha(E)$ spectra were processed using the Athena software following the standard procedures for pre-edge background removal and post-edge normalization.[33,34] The pre-edge peak region was analysed by first subtracting an arctangent background from the normalized XAS spectra of the investigated samples and

then by fitting the pre-edge peak with a sum of Gaussian functions following a consolidated approach.[35] The number of the components used in the fit was chosen as the minimum necessary to reproduce the peaks clearly identifiable in the experimental spectra. All operations associated with the fit decomposition were carried out using the Fytik software without applying any constraint to the peak position, width, and intensity.[36]

3. Results

The morpho-structural properties of the volcanic ash (VA) samples and their transformation into magnetic zeolites during the hydrothermal process were investigated using X-ray diffraction (XRD), and scanning (SEM) and transmission (TEM) electron microscopy. The starting volcanic ashes, as reported in a previous study of the co-authors,[4] upon hydrothermal treatment (see Fig. 2 for the process), show distinct transformations, confirming the conversion from ashes to magnetic zeolites (see XRD analysis in Fig. S1 and S2). SEM analysis further revealed the morphological diversity of the hydrothermally treated samples. Octahedral crystals of X-type zeolite (1–2 μm in size) were prominently identified in the samples treated with distilled water (for example, $VA0H_{60}$ in Fig. 3a). In contrast, the seawater-treated samples were characterized by an abundance of globular grains composed of nanocrystals (for example, $VA0HM_{60}$ in Fig. 3d). Sponge-like masses interspersed with sub-idiomorphic crystals were also observed in several samples, highlighting the morphological complexity induced by the reaction environment. TEM analysis reveals that the treated ashes consist of both crystalline and amorphous material and zeolites (Fig. 3b, e and S3). The 3D periodic channels of X-type zeolites are frequently observed in the $VA0H_{60}$ sample (Fig. 3c), whereas less regular channels are visible in the $VA0HM_{60}$ one (arrow, Fig. 3f). Selected area electron diffraction (SAED) measurements were performed to identify the crystalline phases. Specifically, Fig. 3h shows the SAED pattern of the area shown in Fig. 3g. A unit cell can be identified in the SAED (white dashed line) pattern, whose geometry and interplanar distances corresponding to the diffraction spots ($d_{(-1,-1,3)} = 0.254$ nm; $d_{(5,1,3)} = 0.145$ nm; $d_{(6,0,2)} = 0.133$ nm) indicate the presence of a magnetite crystal in the [−3,9,2] zone-axis orientation. The dark-field image obtained with the diffraction spot encircled in the SAED pattern enables visualization of the corresponding crystal (Fig. 3i).

3.1. Magnetic properties

The temperature dependence of magnetization has been studied by zero-field-cooled (ZFC) and field-cooled (FC) protocols. The ZFC curves of all the VA samples (Fig. 4 upper panel) follow a similar trend that can be described by the occurrence of different magnetic regimes. Starting from low temperature, the first region is characterized by a decrease of the magnetization up to about 25 K that can be ascribed to the paramagnetic behaviour associated with iron ions dispersed within the glassy matrix and/or with paramagnetic iron-containing crystalline phases, confirmed by ICP analysis (Table 2). This is followed by a discontinuity point at about 55 K, and then the curves show an irreversible magnetic behaviour over the explored temperature range, suggesting the presence of a fraction of particles still in a magnetic blocked state at 300 K.[37,38]

From the difference (M_{FC}–M_{ZFC}) we obtained a good approximation of M_{TRM} (thermoremanent magnetization), describing the energy profile of the system.[39,40] The dM_{FC-ZFC}/dT curve is a good estimation of the energy barrier distribution and allows identification of even slight changes in the temperature dependence of magnetization, consistent with the ZFC–FC curves, as shown in Fig. 3 (bottom panel). Interestingly, the dM_{FC-ZFC}/dT curve of all the volcanic ash (VA0, VA1, and VA2) samples showed an intense peak at about 55 K. Since this temperature turned out to be magnetic field-independent (see Fig. S3 in the SI), and given the identification of mainly antiferromagnetic silicate iron-containing phases by XRD, it seems logical to ascribe this to an antiferromagnetic–paramagnetic transition,[3] the temperature being in the range typical of Fe-silica oxides, like fayalite or Fe-containing pyroxenes.[3,41] Although hematite is also present, its Morin transition (~260 K) is not discernible in the $M(T)$ curves, likely due to the dominant

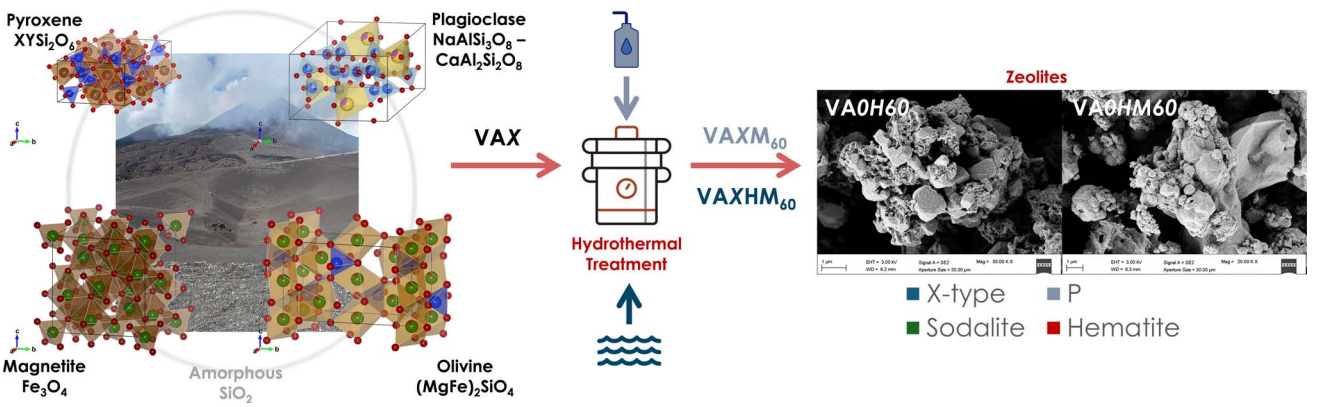

Fig. 2 Transformation from volcanic ashes (*i.e.*, pyroxene, plagioclase, olivine, magnetite, and significant amounts of amorphous silica) to magnetic zeolites (*i.e.*, X-type zeolite, zeolite P, sodalite and hematite) *via* hydrothermal treatment with distilled or seawater. SEM pictures show the morphology of the resulting zeolites.

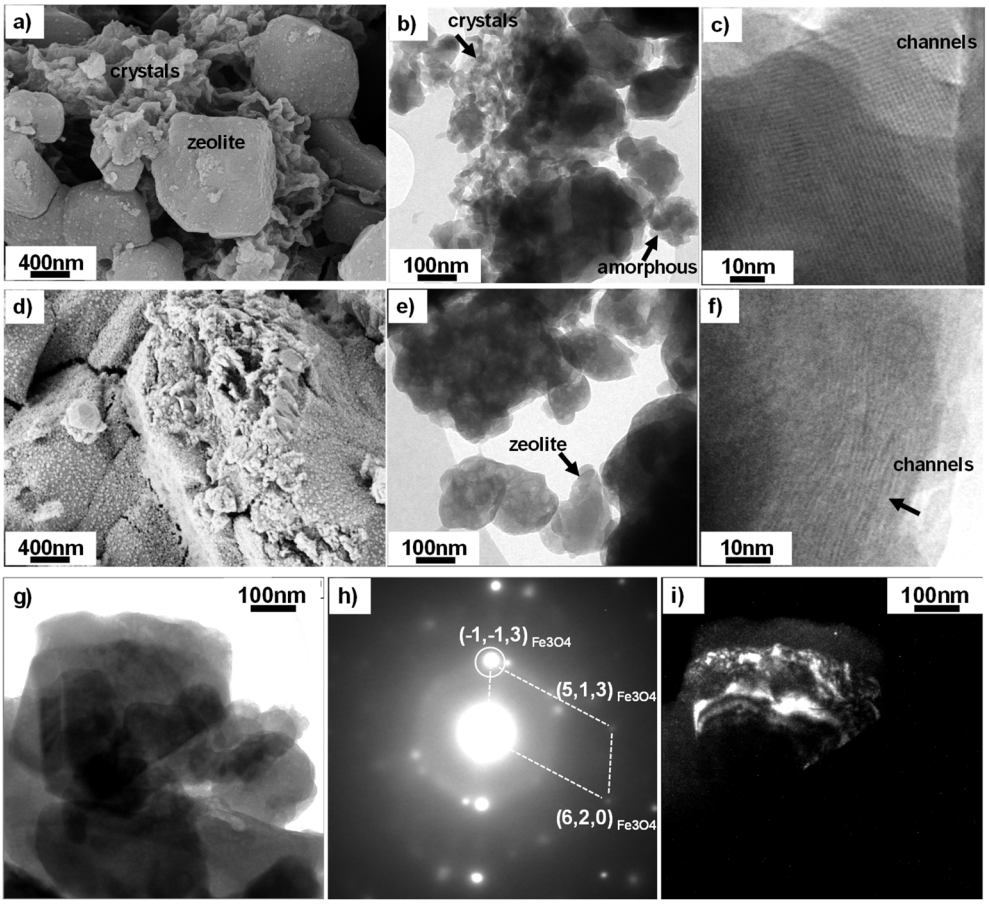

Fig. 3 Sample $VA0H_{60}$: (a) SEM image; (b) and (c) TEM images showing a general view and the 3D channels in a zeolite (arrow), respectively. Sample $VA0HM_{60}$: (d) SEM image; (e) and (f) TEM images showing a general view and the channels in a zeolite; (g–i) are a bright field image, the corresponding SAED pattern, and the dark field image obtained with the circled spot in the SAED pattern, respectively. The white dashed lines identify a unit cell corresponding to a magnetite crystal oriented along the [−3,9,2] zone axis.

magnetic response of other iron oxides and silicate phases, as reported in similar systems.[30,42]

The transformation process of volcanic ashes to magnetic zeolites induces relevant modifications in magnetic properties. The ZFC–FC curves of $VA0H_{60}$ and $VA0HM_{60}$ (5) show the occurrence of a peak typically ascribed to the magnetic relaxation of monodomain ferro (or ferri) MNPs, such as magnetite-like phases.[43] This is accompanied by a wide peak in the derivative of M_{FC}–M_{ZFC} of these samples indicating the blocking temperature of the magnetic mono-domain nanoparticles (*i.e.*, the temperature at which 50% of the particles overcome their anisotropic energy barriers).[44] Despite the differences in the dispersion medium, experimental data indicate that seawater treatment does not significantly affect the intrinsic magnetic properties of the nanoparticles: no clear change in interparticle interaction and in surface effects appears evident. Field dependences of magnetization at 5 K and 300 K has been investigated for all the samples. As an example, *M vs. H* measurement curves of the VA0 series are reported in Fig. 5. VA1 and VA2 series are reported in Fig. S5.

The *M vs. H* curves at 300 K exhibit ferromagnetic-like behaviour (S-shaped curves) indicating that the magnetic behaviour of the samples is dominated by ferro- or ferrimagnetic materials (Fig. 6). The value of the M_s for the VA0 sample is around 10.5 $Am^2\ kg^{-1}$. This value significantly reduced in the samples after hydrothermal treatment to 3.5 and 0.5 $Am^2\ kg^{-1}$ for $VA0H_{60}$ and $VA0HM_{60}$, respectively. However, the hystereses of all the samples exhibit small coercivity, in agreement with the ZFC–FC curve, highlighting the presence of a population of single-domain and/or multidomain particles blocked at room temperature. The hysteresis at 5 K shows an increase of the slope at high field and a ferromagnetic behaviour with $H_c \neq 0$.[45] In particular, the linearity at high field is attributed to the antiferromagnetic-like and/or paramagnetic behaviour, whereas the presence of uncompensated spins can be an indication of the ferrimagnetic-like component, in correlation with the ZFC–FC curves demonstrating the coexistence of paramagnetic, antiferromagnetic, and ferro/ferrimagnetic phases, which are predominant over the others within certain temperature ranges. The antiferromagnetic-like contribution can be reasonably associated with hematite, detected by XRD, whose weak magnetic response is reflected in the linear portion of the hysteresis curves at 5 K. The field dependent magnetization measurements at room and low

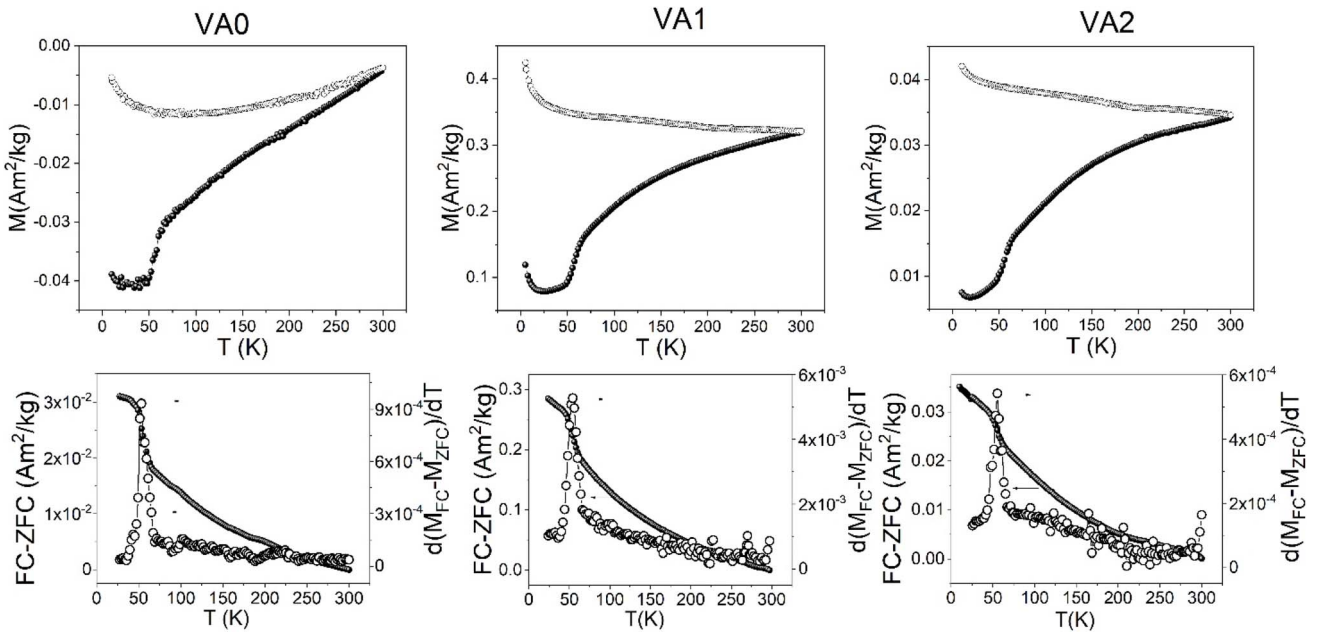

Fig. 4 ZFC FC curves of the VA samples under a magnetic field of 2.5 mT (upper panel); difference $M_{FC}-M_{ZFC}$ curves and the corresponding derivative of ($M_{FC}-M_{ZFC}$) curves (bottom panel).

temperatures for the VA1 and VA2 series show similar magnetic behaviour before and after zeolitization (Fig. S5). All the extracted magnetic parameters are reported in Table 3. In the case of the VA1 series, the process used to obtain zeolites seems to affect the sample slightly differently with respect to VA0 and VA2: the occurrence of the peak in the dM_{FC-ZFC}/dT curve is very weak, but still at the same temperature as for the zeolites obtained from VA0 and VA2, suggesting the same origin, but somehow masked by a higher fraction of fayalite which is not converted during the treatment.

In addition, no Verwey transition around 120 K, typically associated with stoichiometric magnetite,[46] was detected in any of the VA samples. The absence of this feature can be explained by the predominance of fayalite and oxidized ferrimagnetic oxides (γ-Fe_2O_3 and α-Fe_2O_3) evidenced by XRD, together with the likely non-stoichiometric or nanocrystalline character of

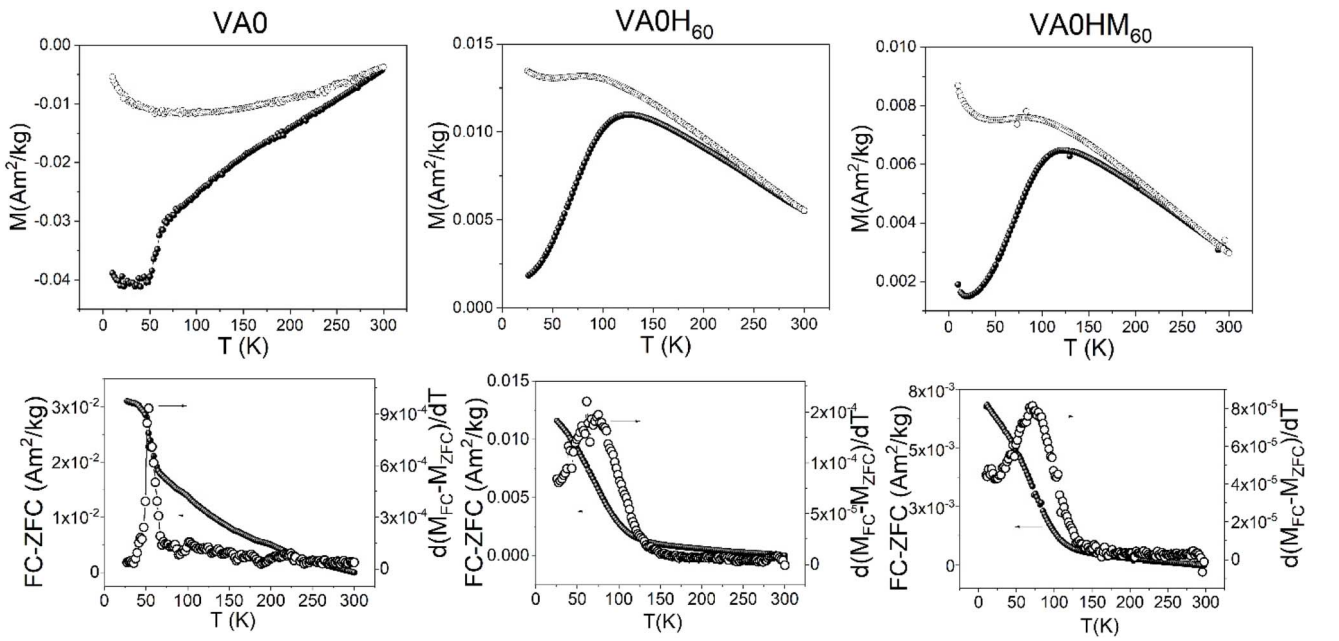

Fig. 5 ZFC/FC curves under a magnetic field of 2.5 mT of the VA0 series (upper panel); difference $M_{FC}-M_{ZFC}$ curves and the corresponding derivative of ($M_{FC}-M_{ZFC}$) (bottom panel).

Table 3 Magnetic parameters, saturation magnetization (M_s), reduced remanent magnetization (M_r/M_s), effective magnetic moment (M_{eff}) and coercive field (H_c) for all the samples (H_c values at 5 K are also reported for comparison)

Sample	M_s at 300 K ($Am^2\ kg^{-1}$)	M_r/M_s at 300 K	M_{eff} at 300 K ($Am^2\ kg^{-1}$)	H_c at 300 K mT	H_c at 5 K mT
VA1	11.5(3)	0.04	8.06(6)	5(3)	19(3)
$VA1H_{60}$	1.5(4)	0.03	0.52(4)	5(3)	15(2)
$VA1HM_{60}$	4.5(2)	0.1	3.03(3)	21(3)	39(2)
VA2	20(2)	0.09	13.5(2)	9(3)	45(5)
$VA2H_{60}$	8.5(3)	0.01	2.5(3)	5(3)	90(2)
$VA2HM_{60}$	7.5(2)	0.06	3.5(3)	8(3)	70(3)
VA0	10.5(3)	0.09	6.5(3)	9(3)	21(2)
$VA0H_{60}$	3.5(5)	0.04	1.5(3)	10(5)	72(2)
$VA0HM_{60}$	0.5(5)	0.02	0.9(2)	8(2)	68(2)

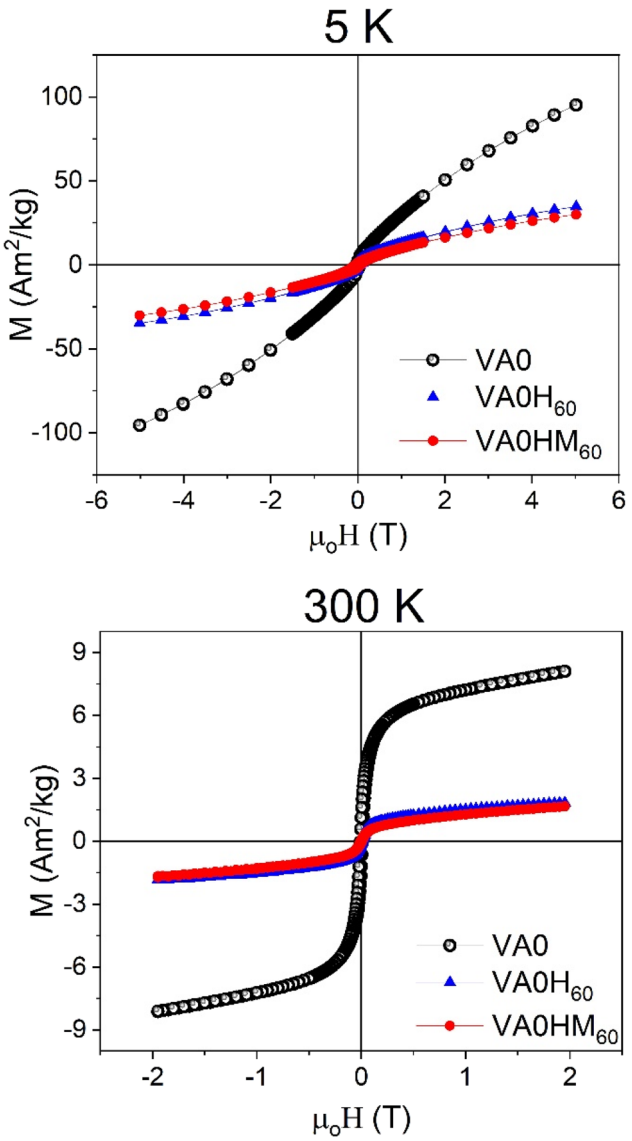

Fig. 6 Field dependence of magnetization curves at 5 K and 300 K for the samples of the VA0 series.

magnetite-like phases, all of which are known to suppress or smear out the transition. Related systems have been shown to display a weak Verwey-like anomaly at low temperature, accompanied by a small hysteresis attributed to magnetite.[47] Similarly, the 300 K hysteresis loops of the VA samples exhibit S-shaped ferromagnetic-like behavior with very low coercivity, while the 5 K loops reveal the coexistence of ferrimagnetic and antiferromagnetic contributions. This confirms that the magnetic response of volcanic ashes is governed by oxidized or non-stoichiometric magnetite-like nanoparticles together with silicate-hosted antiferromagnetic phases.

3.2. XAFS study

To clarify the relationship between the magnetic behaviour and Fe chemical speciation, advanced structural characterization was carried out by Fe–K edge XANES analysis. In fact, the shape of the Fe absorption K-edge curve is strongly influenced by the Fe oxidation state and coordination environment, which is affected by the nearest-neighbour species and their geometry around the absorber atom (tetrahedral, octahedral, or other).[32] Fig. 7a shows the normalized Fe K-edge XANES spectra of all the VA samples and the synthesised magnetic zeolites. The spectra of $VA1H_{60}$ and $VA1HM_{60}$ are broadened in the post-edge region, with respect to VA1, suggesting that the hydrothermal procedure using either distilled water or seawater has affected the local structure of iron in volcanic ashes. This effect is also evident in the spectra of the VA2 and VA0 series. It is worth noting that there is a positive chemical shift of the absorption edge position in $VA1H_{60}$, $VA1HM_{60}$ and the other magnetic zeolites, indicating that the oxidation state of iron has increased after the hydrothermal process. Additional variations are also visible in the edge region, the shape of the absorption maximum and both the intensity and energy position of the pre-edge peaks (Fig. 7b). These changes are related to a variation in the Fe oxidation state and local structure, in response to the synthesis procedure.

The relevant parameter to infer the oxidation state of Fe is the energy position of the centroid of the pre-edge features, which is related to the 1s–3d electronic transitions,[32] and this transition is dipole-forbidden. However, the hybridization of Fe-3d states with oxygen-p states favors the probability for some dipole-allowed transition. The p–d hybridization depends on the FeO coordination symmetry, *i.e.* it is negligible in the FeO_6 octahedral (O_h) symmetry while it is high in the FeO_4 tetrahedral (T_d) symmetry.[48] Distortions out of the O_h symmetry

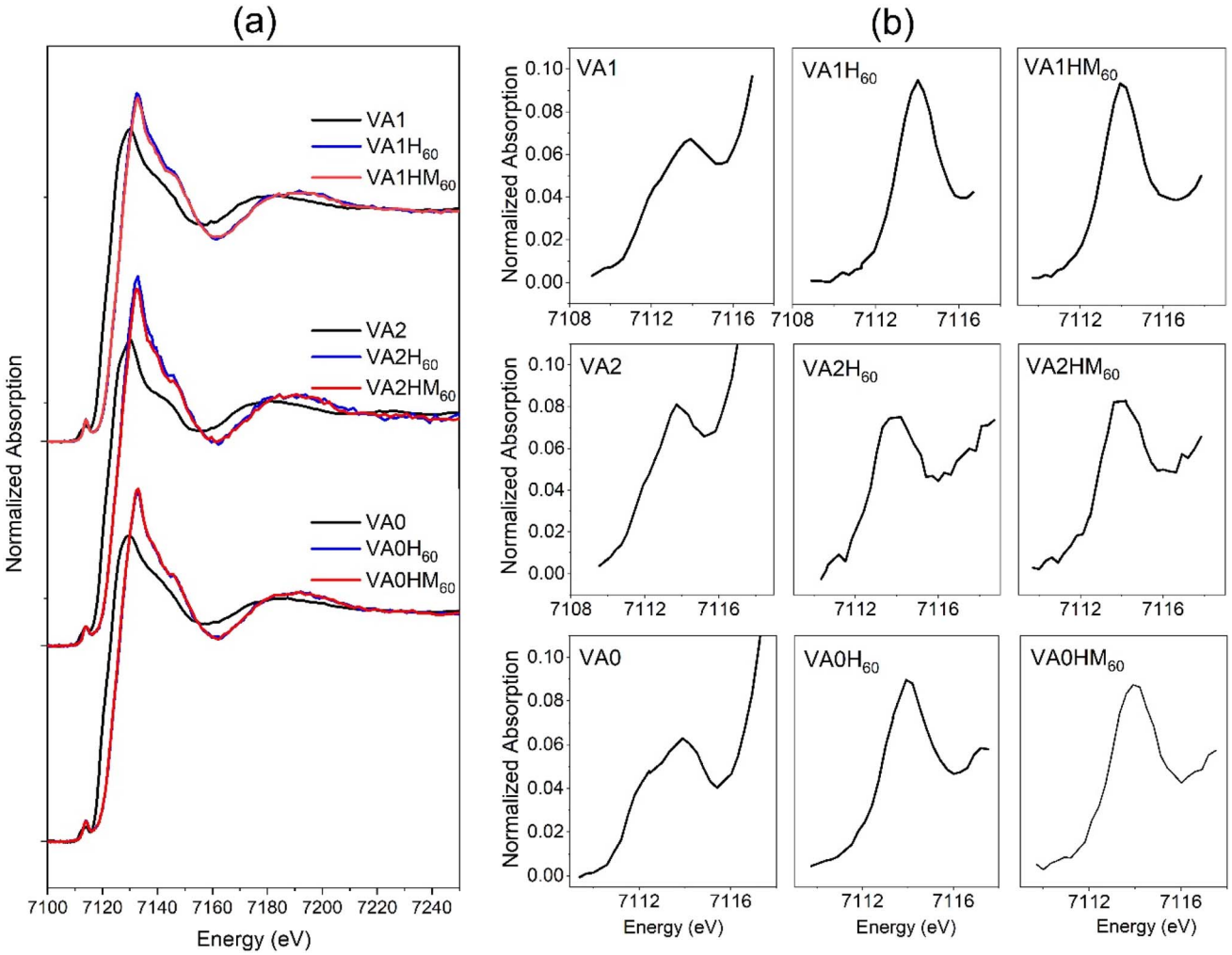

Fig. 7 (a) Experimental Fe K-edge XANES spectra; (b) close look at the pre-edge region of all the samples.

provide some superposition between Fe-3d and O-p states, thus enhancing the pre-edge peak intensity. This implies that the pre-edge peak energy position and intensity are greatly affected by the average Fe oxidation state and coordination geometry.[49,50] These features provide a simple way to estimate the FeO average coordination symmetry and average coordination number. Moreover, the average coordination number can be inferred from the intensity (or integrated area) of the centroid.

Following a consolidated approach, the pre-edge peaks along with the Gaussian component used in the fitting procedures (after background subtraction) are shown in Fig. 8. It was observed that the spectra of the volcanic ashes exhibit a two-component pre-edge feature, while after zeolitization the peaks merge into a single intense peak. The pre-edge peak of the VA1 sample was fitted accordingly with two components whose energies (~7111.8 and 7113.7 eV) are fairly consistent with those of Fe in a silica matrix compound, while the first and the second features were ascribed to contributions from Fe^{2+} and Fe^{3+}, respectively.[15] The first peak reflected all the features of the 1s → 3d pre-edge region typical of low-spin ferrous reference complexes.[51] All the VA samples have an octahedral iron site, and therefore, the only intensity mechanism for the 1s → 3d pre-edge feature is the allowed electric quadrupole transition. The $^1A_{1g}$ ground state of these low-spin ferrous complexes has an electronic hole configuration of e_g^4, with e_g^3 being the only allowed excited hole configuration (Fig. 9a). The e_g^3 hole configuration produces a ^2E_g excited many-electron state giving rise to a single pre-edge feature at lower energy.[28] On the high-energy side of the pre-edge, the presence of an unsplitted feature at ~7114 eV indicated an apparent major contribution of Fe^{3+}. These peaks correspond to the pre-edge features of a high-spin ferric tetrahedral complex which is a signature of the presence of neighbouring pairs of Fe^{3+}. The 1s → 3d pre-edge feature of these complexes gains intensity both from the allowed electric quadrupole mechanism and from the electric dipole mechanism associated with the hybridization of 4p orbitals into 3d orbitals. In the high-spin ferric octahedral case, there are two one-electron allowed excited hole configurations, $(t_2)^2(e)^2$ and $(t_2)^3(e)^1$ (Fig. 9b), which produce two many-electron states, $^5T_2$ and ^5E, respectively. The two contributions from Fe^{2+} and Fe^{3+} oxidation states are separated by 2 eV which contribute to the total pre-edge in the VA samples.

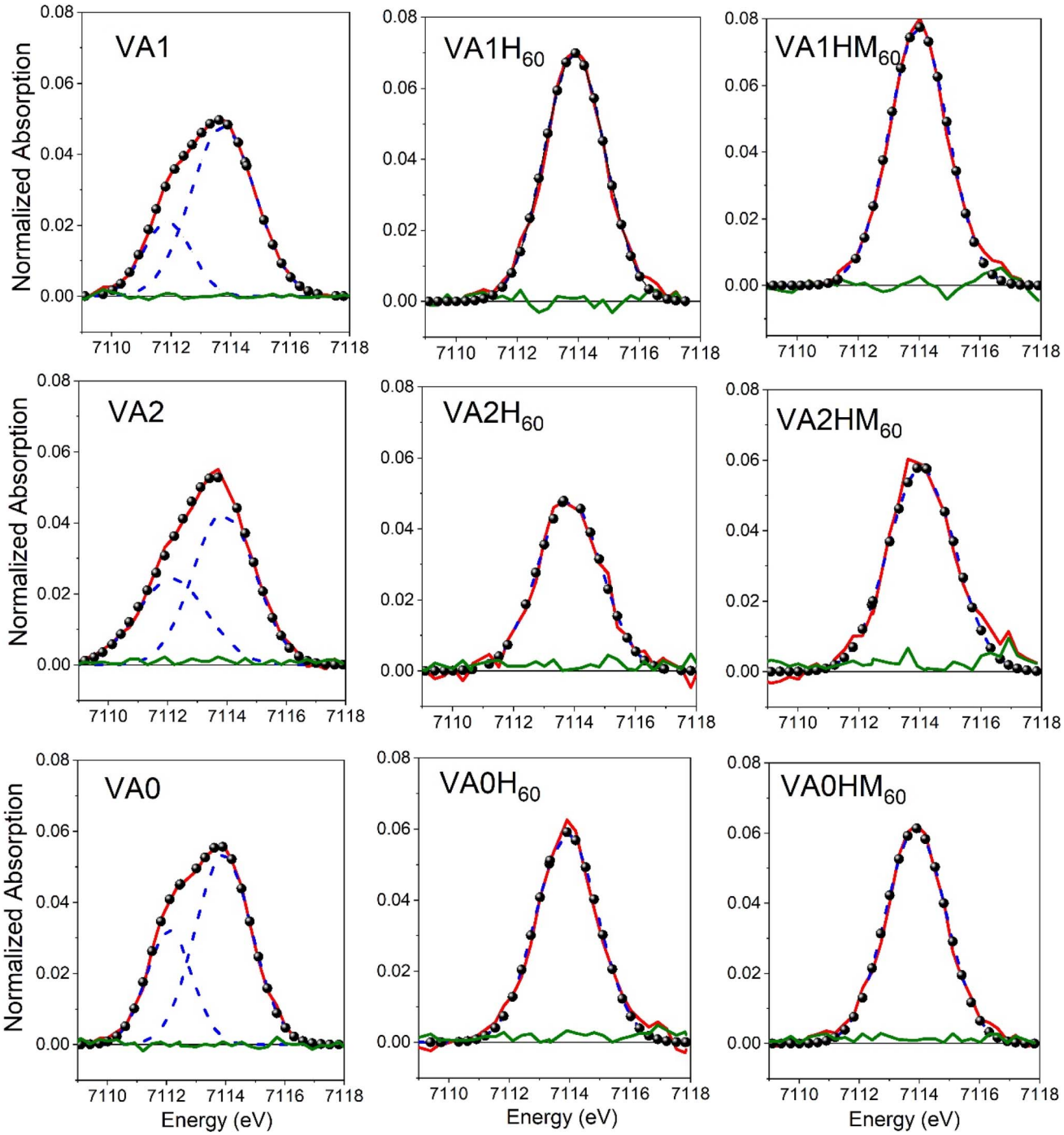

Fig. 8 Background subtracted pre-edge peaks of the samples obtained after the subtraction of an arctangent curve mimicking the absorption edge (red line), the Gaussian components used to fit the pre-edge peak (blue dashed lines), and the best fit to the data (black solids) and the residual (green line).

On the other hand, the magnetic zeolites synthesised from volcanic ashes showed a pre-edge feature that displays an intense peak at the same energy of the second peak in the pre-edge of the volcanic ashes (~7114 eV). The centroid position of this peak is the same as Fe^{3+} reference compounds indicating that during the formation of zeolites Fe^{2+} components in volcanic ashes converted to Fe^{3+}. The pre-edge features of a high-spin ferric tetrahedral complex gain intensity from 4p mixing into the 3d orbitals. Since the 4p orbitals transform as t_2, only mixing into the 3d t_2 set contributes to the intensity of the transition into the $^5T_2$ state.

In particular, accurate evaluation of the pre-edge peak centroid energy and integrated intensity compared with those of Fe model compounds can provide quantitative information

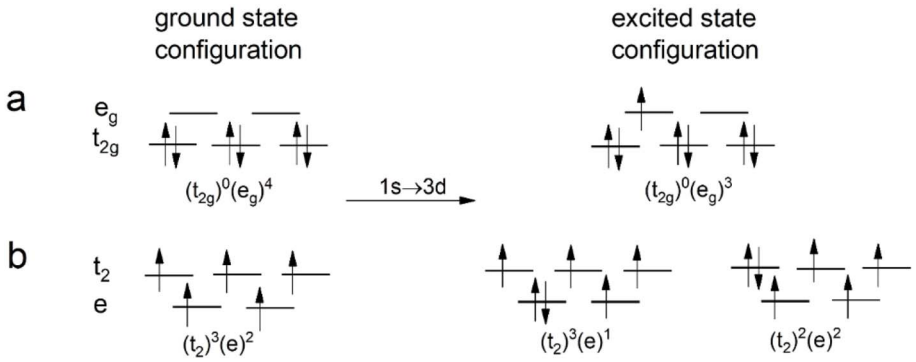

Fig. 9 (a and b) The electronic configuration at ground and excited states for the 1s to 3d excitation mode.

Table 4 Pre-edge peak data of the Fe K-edge XANES spectra of all the samples

Sample	Centroid (eV)	Integrated intensity	Fit agreement index (%)
VA1	7113.4	0.17	99.84
$VA1H_{60}$	7113.0	0.19	99.32
$VA1HM_{60}$	7113.9	0.17	99.35
VA2	7113.2	0.18	99.75
$VA2H_{60}$	7113.8	0.13	99.53
$VA2HM_{60}$	7114.1	0.16	99.35
VA0	7113.3	0.18	99.42
$VA0H_{60}$	7113.9	0.15	99.31
$VA0HM_{60}$	7113.9	0.15	99.45

on both the Fe oxidation state and coordination environment where its intensity will be minimal in the case of regular octahedral symmetry around the absorber, whereas it will reach its maximum in the tetrahedral case.[52] This analysis can be provided with the energy *vs.* oxidation state/coordination number calibration curve using the energy position and intensity of the centroid of the pre-edge peaks of Fe^{2+} and Fe^{3+} reference compound spectra (Table 4). The integrated intensity of the pre-edge peaks is plotted as a function of their centroid energies in Fig. 10. A clear trend is depicted: in pristine VA0, VA1 and VA2 samples the integrated areas of the pre-edge peak are representative of domination of glassy Fe^{2+}, and the Fe–O coordination number is found to be between 4 and 5. In contrast, the pre-edge centroid for all the zeolite samples clearly shifted by about 1 eV coming close to the region of Fe^{3+} 5-coordinated compounds.[16]

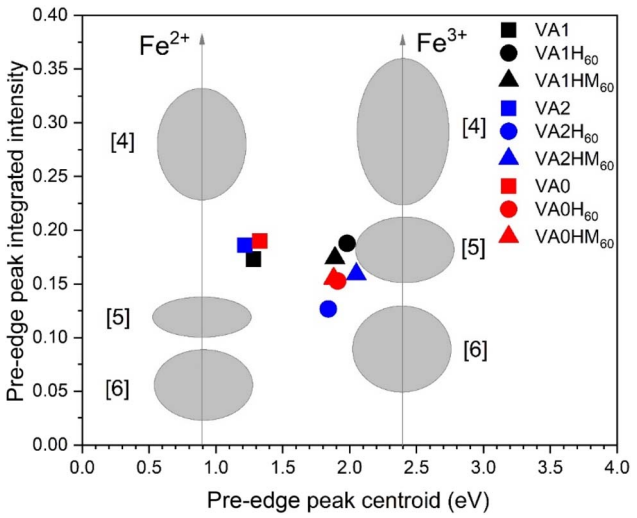

Fig. 10 Plot of the background subtracted pre-edge peak integrated intensity *vs.* centroid energy position of all the samples. Zero energy refers to the first maximum of the first derivative of the metallic Fe spectrum.

4. Discussion

Combining Fe XANES analysis with magnetic characterization allows better understanding of the behaviour of Fe in complex matrices before and after the hydrothermal treatment. If we consider the derivative of FC–ZFC in Fig. 4 the intense peak at about 55 K in volcanic ash samples could be ascribed to a magnetic phase transition from antiferromagnetic (low T) to a paramagnetic behaviour (high T).[3] In this framework, the X-ray diffraction patterns of the volcanic ashes were meticulously re-examined. Among the detected phases—pyroxene, feldspars, olivine, and magnetite/maghemite—only iron integrated into a silica oxide complex aligns with the Néel temperature observed in our experimental magnetic and XAS data.[53] The magnetic transition observed in the FC–ZFC curves is consistent with the behaviour of fayalite (Fe_2SiO_4), the Fe-rich endmember of the forsterite–fayalite solid solution series. Fayalite typically exhibits a broad magnetic transition at approximately 65 K,[54] in agreement with the experimental results. In contrast, forsterite (Mg_2SiO_4), the Mg-rich endmember, is diamagnetic. As the magnesium-to-iron ratio increases, transitioning from fayalite toward forsterite, the magnetic transition temperature decreases.[55] This interpretation is further supported by the findings of Geiger *et al.*, who reported a Néel temperature of 55 K for $Fa_{80}Fo_{20}$ (80% fayalite and 20% forsterite).[41] Thus, the hypothesis that iron within a silica oxide complex acts as the antiferromagnetic phase responsible for the observed magnetic features agrees well with both experimental and literature data.

After zeolitization, Fe^{2+} atoms in fayalite could be likely transformed into Fe^{3+} of hematite, as well as magnetite-like phases, owing to the oxidizing conditions (see equations later). This hypothesis is strongly supported by the evolution of pre-edge regions of Fe XANES spectra, which reveal the increase in the oxidation state of iron. Although its structure (confirmed by TEM) and valence state (confirmed by XANES) are consistent with magnetite, the absence of a detectable Verwey transition, likely due to chemical substitution,[56] oxidation,[57] and surface modification,[58] precludes unambiguous identification based solely on magnetic measurements. The proposed mechanism is that fayalite will be oxidised to hematite (Fe_2O_3), magnetite (Fe_3O_4) and silica (SiO_2) according to the following equations:[59]

$$2FeO\cdot SiO_2 + 1/2O_2 \rightarrow Fe_2O_3 + SiO_2 \quad (1)$$

$$2FeO\cdot SiO_2 + 1/3O_2 \rightarrow 2/3Fe_3O_4 + SiO_2 \quad (2)$$

Exposing fayalite in water at high temperature (as in our case) provides a catalytic surface for water adsorption. Water molecules first undergo a physisorption process and upon interaction between Fe 3d-orbitals and water O 2p-orbitals, a weak substrate–adsorbate bond is created. Subsequently, water molecules dissociate into OH and H surface species, where the OH groups reside on the metal atoms, the H species are attached to the surface O atoms and OH dissociates to produce adsorbed oxygen atoms.[60,61] It should be underlined that this process also marginally involves pyroxenes.

Moreover, the fusion of volcanic ashes at high temperature with NaOH is the reason for the partial conversion of fayalite to hematite, during the synthesis of zeolites. The preliminary evidence of this transition, observed through the reduction of the intensity of peaks of fayalite in X-ray diffraction patterns of the magnetic zeolites and the consequent increase of the intensity of peaks related to hematite (Fig. S2), is supported by the changing magnetic behaviour of volcanic ashes after treatment. Firstly, the saturation magnetization decreased moving from the volcanic ashes to the magnetic zeolites. The significant reduction clearly confirmed the increase of the antiferromagnetic hematite phase (the expected value of the effective magnetic moment for pure nanostructured hematite is <0.5 $Am^2\ kg^{-1}$).[62,63] Secondly, NaOH leads to the disruption of the silica network, and subsequent production and diffusion of more water molecules, promoting the oxidation of fayalite and magnetite, according to the following reaction:

$$2NaOH + xSiO_2 \rightarrow Na_2O\cdot xSiO_2 + H_2O \quad (3)$$

Under these conditions, iron oxide mainly exists in the form of hematite with a small amount of magnetite-like phases as intermediate reaction products, due to the high oxygen partial pressure. The presence of maghemite cannot be ruled out. These results are strongly supported by the XAS analysis suggesting a change in the coordination number for iron. As a matter of fact, the disappearing intense antiferromagnetic–paramagnetic transition visible in the FC–ZFC curves of magnetic zeolite, confirms the presence of olivine with a higher ratio of fayalite ($Fa_{80}Fo_{20}$) in the FC–ZFC curves of the starting VA samples.

5. Conclusion

This work sheds some light on the mechanism of a sustainable and high-yield strategy to convert volcanic ash from Mount Etna—rich in olivine and other iron-containing silicates—into magnetically active zeolitic materials *via* hydrothermal treatment. The pristine ash displays mixed magnetic features arising from the coexistence of ferri/ferromagnetic and paramagnetic phases. Hydrothermal processing induces both structural and magnetic transformations. At 60 °C, zeolitic crystallization occurs while retaining magnetic functionality, and promoting partial conversion of olivine into hematite, leading to a reduction in magnetization, and to magnetite-like phases. These trends are supported by Fe K-edge XAS, which confirms the evolution of iron speciation. Overall, this work highlights the value of volcanic waste as a low-cost feedstock for the production of functional materials with potential applications in magnetic separation, catalysis, and environmental remediation—offering a resource-efficient and circular pathway for advanced material design.

Author contributions

Maryam Abdolrahimi: formal analysis, investigation, visualization, writing – original draft, review & editing. Pierfrancesco Maltoni: formal analysis, investigation, visualization, writing – review & editing. Gianni Barucca: formal analysis, methodology, writing – review & editing. Claudia Belviso: conceptualization, funding acquisition, investigation, writing – review & editing. Carlo Meneghini: formal analysis, investigation, supervision, writing – review & editing. Davide Peddis: conceptualization, funding acquisition, supervision, writing – review & editing.

Conflicts of interest

The authors declare that they have no competing interests.

Data availability

The data supporting this article have been included as part of the manuscript.

Supplementary information is available. See DOI: **https://doi.org/10.1039/d5ta03456f**.

Acknowledgements

DP and MA acknowledge the project funded under the National Recovery and Resilience Plan (NRRP), Mission 4 Component 2 Investment 1.3 – Call for tender No. 1561 of 11.10.2022 of Ministero dell'Università e della Ricerca (MUR); funded by the European Union – Next Generation EU • Award Number: Project code PE0000021, Concession Decree No. 1561 of 11.10.2022 adopted by Ministero dell'Università e della Ricerca (MUR), and CUP D33C22001330002 –Project title "Network 4 Energy

Sustainable Transition – NEST". Thanks to Elettra Synchrotron and the SIM beamline for providing the facilities and support for the XAS measurements. Pictures of Mt. Etna are courtesy of P. Maltoni and L. Catanzaro.

References

1 G. A. Waychunas, C. S. Kim and J. F. Banfield, Nanoparticulate iron oxide minerals in soils and sediments: Unique properties and contaminant scavenging mechanisms, *J. Nanopart. Res.*, 2005, **7**(4–5), 409–433, DOI: 10.1007/s11051-005-6931-x.

2 E. Murad, Magnetic properties of microcrystalline iron (III) oxides and related materials as reflected in their Mössbauer spectra, *Phys. Chem. Miner.*, 1996, **23**(4–5), 248–262, DOI: 10.1007/bf00207766.

3 V. Mameli, A. Musinu, D. Niznansky, *et al.*, Much more than a glass: The complex magnetic and microstructural properties of obsidian, *J. Phys. Chem. C*, 2016, **120**(48), 27635–27645, DOI: 10.1021/acs.jpcc.6b08387.

4 C. Belviso, M. Abdolrahimi, D. Peddis, *et al.*, Synthesis of zeolite from volcanic ash: Characterization and application for cesium removal, *Microporous Mesoporous Mater.*, 2021, **319**, 111045, DOI: 10.1016/j.micromeso.2021.111045.

5 R. M. Cornell and U. Schwertmann, *The Iron Oxides: Structure, Properties, Reactions, Occurences and Uses*, Wiley-VCH, Weinheim, 2003, DOI: 10.1002/3527602097.

6 P. Robinson, R. J. Harrison, S. A. McEnroe and R. B. Hargraves, Lamellar magnetism in the haematite-ilmenite series as an explanation for strong remanent magnetization, *Nature*, 2002, **418**(6897), 517–520, DOI: 10.1038/nature00942.

7 A. R. Loiola, R. A. Bessa, C. P. Oliveira, *et al.*, Magnetic zeolite composites: Classification, synthesis routes, and technological applications, *J. Magn. Magn. Mater.*, 2022, **560**, 169651, DOI: 10.1016/j.jmmm.2022.169651.

8 C. Belviso, F. Cavalcante, P. Ragone and S. Fiore, Immobilization of Ni by synthesising zeolite at low temperatures in a polluted soil, *Chemosphere*, 2010, **78**(9), 1172–1176, DOI: 10.1016/j.chemosphere.2009.12.046.

9 A. Imran, E. A. Bramer, K. Seshan and G. Brem, Catalytic flash pyrolysis of biomass using different types of zeolite and online vapor fractionation, *Energies*, 2016, **9**(3), 1–17, DOI: 10.3390/en9030187.

10 C. Belviso, F. Cavalcante, S. Di Gennaro, *et al.*, Removal of Mn from aqueous solution using fly ash and its hydrothermal synthetic zeolite, *J. Environ. Manage.*, 2014, **137**, 16–22, DOI: 10.1016/j.jenvman.2014.01.040.

11 C. Belviso, F. Cavalcante, P. Ragone and S. Fiore, Immobilization of Zn and Pb in polluted soil by in situ crystallization zeolites from fly ash, *Water, Air, Soil Pollut.*, 2012, **223**(8), 5357–5364, DOI: 10.1007/s11270-012-1285-3.

12 S. Gjyli, A. Korpa, T. Tabanelli, R. Trettin, F. Cavani and C. Belviso, Higher conversion rate of phenol alkylation with diethylcarbonate by using synthetic fly ash-based zeolites, *Microporous Mesoporous Mater.*, 2019, **284**, 434–442, DOI: 10.1016/j.micromeso.2019.04.065.

13 A. Shahzad, B. Aslibeiki, S. Slimani, *et al.*, Magnetic nanocomposite for lead (II) removal from water, *Sci. Rep.*, 2024, **14**(1), 1–12, DOI: 10.1038/s41598-024-68491-8.

14 P. Maltoni, G. Varvaro, N. Yaacoub, G. Barucca, J. P. Miranda-Murillo, J. Tirabzonlu, S. Laureti, D. Fiorani, R. Mathieu, A. Omelyanchik and D. Peddis, Structural and Magnetic Properties of $CoFe_2O_4$ Nanoparticles in an α-Fe_2O_3 Matrix, *J. Phys. Chem. C*, 2025, **129**, 591–599, DOI: 10.1021/acs.jpcc.4c05320.

15 G. Giuli, R. Alonso-Mori, M. R. Cicconi, *et al.*, Amorphous materials: Properties, structure, and durability: Effect of alkalis on the Fe oxidation state and local environment in peralkaline rhyolitic glasses, *Am. Mineral.*, 2012, **97**(2–3), 468–475, DOI: 10.2138/am.2012.3888.

16 F. Bardelli, G. Giuli, F. Di Benedetto, *et al.*, Spectroscopic study of volcanic ashes, *J. Hazard. Mater.*, 2020, **400**, 123213, DOI: 10.1016/j.jhazmat.2020.123213.

17 T. Tobase, A. Yoshiasa, L. Wang, *et al.*, XAFS study of Zr in Cretaceous-Tertiary boundary clays from Stevns Klint, *J. Mineral. Petrol. Sci.*, 2015, **110**(2), 88–91, DOI: 10.2465/jmps.141022a.

18 J. Régnard, J. Chappert, J. Régnard, J. C. Mössbauer, S. Of, and N. Glasses, *Mössbauer Study Of Natural Glasses : Lipari And Teotihuacan Obsidians To Cite This Version : Hal Id : JPA-00219789*, 1980.

19 E. Schmidbauer, E. Mosheim and N. Semioschkina, Magnetization and 57Fe Mössbauer study of obsidians, *Phys. Chem. Miner.*, 1986, **13**(4), 256–261, DOI: 10.1007/BF00308277.

20 S. J. Stewart, G. Cernicchiaro, R. B. Scorzelli, G. Poupeau, P. Acquafredda and A. De Francesco, Magnetic properties and 57Fe Mössbauer spectroscopy of Mediterranean prehistoric obsidians for provenance studies, *J. Non-Cryst. Solids*, 2003, **323**(1–3), 188–192, DOI: 10.1016/S0022-3093(03)00305-3.

21 W. Luo, W. Cao, P. C. A. Bruijnincx, L. Lin, A. Wang and T. Zhang, Zeolite-supported metal catalysts for selective hydrodeoxygenation of biomass-derived platform molecules, *Green Chem.*, 2019, **21**(14), 3744–3768, DOI: 10.1039/c9gc01216h.

22 S. Buzukashvili, R. Sommerville, O. Kökkılıç, P. Ouzilleau, N. A. Rowson and K. E. Waters, Exploring efficiency and regeneration of magnetic zeolite synthesized from coal fly ash for water treatment applications, *JCIS Open*, 2025, **17**, 100127, DOI: 10.1016/j.jciso.2024.100127.

23 Y. Yuan, F. J. Wu, S. T. Xiao, *et al.*, Hierarchical zeolites containing embedded Cd0.2Zn0.8S as a photocatalyst for hydrogen production from seawater, *Chem. Commun.*, 2023, 7275–7278, DOI: 10.1039/d3cc01409f.

24 I. Khan, A. Altaf, S. Sadiq, *et al.*, Towards sustainable solutions: Comprehensive review of advanced porous materials for CO_2 capture, hydrogen generation, pollutant degradation, and energy application, *Chem. Eng. J. Adv.*, 2025, **21**, 100691, DOI: 10.1016/j.ceja.2024.100691.

25 A. Hagan, F. S. Stone, and J. C. Vickerman, *Magnetic Studies of Zeolites*, 1971.

26 A. G. Valencia-Huaman, S. H. Fuentes-Mamani, L. F. Mamani-De La Cruz, *et al.*, Obtaining Zeolites from Natural Materials of Volcanic Origin for Application in Catalytic Pyrolysis for the Sustainable Chemical Recycling of Polymers, *Sustainability*, 2024, **16**(14), 1–15, DOI: 10.3390/su16145910.

27 M. G. Samant, J. Stöhr, H. R. Brown, T. P. Russell, J. M. Sands and S. K. Kumar, NEXAFS studies on the surface orientation of buffed polyimides, *Macromolecules*, 1996, **29**(26), 8334–8342, DOI: 10.1021/ma951820c.

28 T. E. Westre, P. Kennepohl, J. G. Dewitt, B. Hedman, K. O. Hodgson and E. I. Solomon, A Multiplet Analysis of Fe K-Edge 1s f 3d Pre-Edge Features of Iron Complexes, *J. Am. Chem. Soc.*, 1997, **7863**(20), 6297–6314, DOI: 10.1021/ja964352a.

29 U. Wongpratat, S. Maensiri and E. Swatsitang, EXAFS study of cations distribution dependence of magnetic properties in Co1-xZnxFe2O4 nanoparticles prepared by hydrothermal method, *Microelectron. Eng.*, 2015, **146**, 68–75, DOI: 10.1016/j.mee.2015.03.059.

30 Ö. Özdemir, D. J. Dunlop and T. S. Berquó, Morin transition in hematite: Size dependence and thermal hysteresis, *Geochem., Geophys., Geosyst.*, 2008, **9**(10), 1–12, DOI: 10.1029/2008GC002110.

31 A. Di Cicco, G. Aquilanti, M. Minicucci, *et al.*, Novel XAFS capabilities at ELETTRA synchrotron light source, *J. Phys.:Conf. Ser.*, 2009, **190**(1), 012043, DOI: 10.1088/1742-6596/190/1/012043.

32 M. Wilke, F. Farges, P. E. Petit, G. E. Brown and F. Martin, Oxidation state and coordination of Fe in minerals: An Fe K-XANES spectroscopic study, *Am. Mineral.*, 2001, **86**(5–6), 714–730, DOI: 10.2138/am-2001-5-612.

33 B. Ravel and M. Newville, ATHENA, ARTEMIS, HEPHAESTUS: Data analysis for X-ray absorption spectroscopy using IFEFFIT, *J. Synchrotron Radiat.*, 2005, **12**(4), 537–541, DOI: 10.1107/S0909049505012719.

34 B. Ravel and M. Newville, ATHENA and ARTEMIS: Interactive graphical data analysis using IFEFFIT, *Phys. Scr., T*, 2005, **T115**, 1007–1010, DOI: 10.1238/Physica.Topical.115a01007.

35 G. Gabriele, P. Giovanni and C. E. P. Curzio, Iron local structure in tektites and impact glasses by extended X-ray absorption fine structure and high-resolution X-ray absorption near-edge structure spectroscopy, *Geochim. Cosmochim. Acta*, 2002, **66**(24), 4347–4353.

36 W. M. Fityk, A general-purpose peak fitting program, *J. Appl. Crystallogr.*, 2010, **43**(5 PART 1), 1126–1128, DOI: 10.1107/S0021889810030499.

37 C. Cannas, D. Gatteschi, A. Musinu, G. Piccaluga and C. Sangregorio, Structural and magnetic properties of Fe_2O_2 nanoparticles dispersed over a silica matrix, *J. Phys. Chem. B*, 1998, **102**(40), 7721–7726, DOI: 10.1021/jp981355w.

38 F. Chávez-Rivas, R. Zamorano-Ulloa, D. Galland, J. R. Regnard and J. Chappert, Ferro and paramagnetic resonance studies of natural volcanic glasses: Teotihuacan obsidians, *J. Appl. Phys.*, 1991, **70**(10), 5849–5851, DOI: 10.1063/1.350133.

39 E. H. El-Hilo and K. O'Grady, Spin-glass behavior in a fine particle system, *IEEE Trans. Magn.*, 1991, **27**(4), 3570–3578, DOI: 10.1109/20.102929.

40 G. Muscas, F. Congiu and G. Concas, The Boundary Between Volume and Surface-Driven Magnetic Properties in Spinel Iron Oxide Nanoparticles, *Nanoscale Res. Lett.*, 2022, **17**(1), 98, DOI: 10.1186/s11671-022-03737-w.

41 C. A. Geiger, M. Grodzicki and E. Dachs, An analysis of the magnetic behavior of olivine and garnet substitutional solid solutions, *Am. Mineral.*, 2019, **104**(9), 1246–1255, DOI: 10.2138/am-2019-6839CCBYNCND.

42 L. D. L. S. Valladares, A. Vargas-Luque, L. Borja-Castro, *et al.*, Physical and chemical techniques for a comprehensive characterization of river sediment: A case of study, the Moquegua River, Peru, *Int. J. Sediment Res.*, 2024, **39**(3), 478–494, DOI: 10.1016/j.ijsrc.2024.03.003.

43 A. Talone, P. Maltoni, M. Casale, *et al.*, Novel Formulation of Ionic Liquid-Based Ferrofluids: Investigation of the Magnetic Properties, *Langmuir*, 2025, **41**(19), 11977–11986, DOI: 10.1021/acs.langmuir.5c00403.

44 K. L. Livesey, S. Ruta, N. R. Anderson, D. Baldomir, R. W. Chantrell and D. Serantes, Beyond the blocking model to fit nanoparticle ZFC/FC magnetisation curves, *Sci. Rep.*, 2018, **8**(1), 1–9, DOI: 10.1038/s41598-018-29501-8.

45 L. Suber, R. Zysler, A. GarcÍa Santiago, *et al.*, Size and Shape Effect on the Magnetic Properties of α-Fe_2O_3 Nanoparticles, *Mater. Sci. Forum*, 1998, **269–272**, 937–942, DOI: 10.4028/www.scientific.net/msf.269-272.937.

46 F. Walz, The Verwey transition - a topical review, *J. Phys.:Condens. Matter*, 2002, **14**(12), R285, DOI: 10.1088/0953-8984/14/12/203.

47 L. D. L. S. Valladares, J. H. J. Kooyip, L. E. Borja-Castro, *et al.*, Characterization of Spanish River Carbonatite (SRC) for agricultural fertilizer, *Hyperfine Interact.*, 2022, **243**(1), 5–10, DOI: 10.1007/s10751-022-01803-4.

48 S. Mobilio, F. Boscherini and C. Meneghini, *Synchrotron Radiation*, Springer Heidelberg New York Dordrecht London, 1997, vol. 29, DOI: 10.1016/S0076-695X(08)60611-0.

49 G. E. Brown, F. Farges and G. Calas, X-ray scattering and X-ray spectroscopy studies of silicate melts, *Mineral. Geochem.*, 1995, **32**, 317–410.

50 G. Calas and J. Petiau, Coordination of iron in oxide glasses through high-resolution K-edge spectra: Information from the pre-edge, *Solid State Commun.*, 1983, **48**(7), 625–629, DOI: 10.1016/0038-1098(83)90530-6.

51 L. Galoisy, G. Calas and M. A. Arrio, High-resolution XANES spectra of iron in minerals and glasses: Structural information from the pre-edge region, *Chem. Geol.*, 2001, **174**(1–3), 307–319, DOI: 10.1016/S0009-2541(00)00322-3.

52 N. V. R. A. Dharanipragada, V. V. Galvita, H. Poelman, C. Lukas and G. B. M. Buelens, Insight in Kinetics from Pre-Edge Features Using Time Resolved in situ XAS, *Am. Inst. Chem. Eng.*, 2018, **64**(4), 1339–1349, DOI: 10.1002/aic.16017.

53 C. P. Hunt, B. M. Moskowitz and S. K. Banerjee, Magnetic Properties of Rocks and Minerals: A Handbook of Physical

Constants, *Rock Phys Phase Relations*, 1995, vol. 3, pp. 189–204, DOI: 10.1016/B978-0-444-53802-4.00048-8.

54 R. P. Santoro, R. E. Newnham and S. Nomura, Magnetic properties of Mn2SiO4 and Fe2SiO4, *J. Phys. Chem. Solids*, 1966, **27**(4), 655–666, DOI: 10.1016/0022-3697(66)90216-2.

55 F. Belley, E. C. Ferré, F. Martín-Hernández, M. J. Jackson, M. D. Dyar and E. J. Catlos, The magnetic properties of natural and synthetic (Fex, Mg1 - x)2 SiO4 olivines, *Earth Planet. Sci. Lett.*, 2009, **284**(3–4), 516–526, DOI: 10.1016/j.epsl.2009.05.016.

56 J. Santoyo Salazar, L. Perez, O. De Abril, *et al.*, Magnetic iron oxide nanoparticles in 10-40 nm range: Composition in terms of magnetite/maghemite ratio and effect on the magnetic properties, *Chem. Mater.*, 2011, **23**(6), 1379–1386, DOI: 10.1021/cm103188a.

57 T. Kim, S. Sim, S. Lim, *et al.*, Slow oxidation of magnetite nanoparticles elucidates the limits of the Verwey transition, *Nat. Commun.*, 2021, **12**(1), 10–15, DOI: 10.1038/s41467-021-26566-4.

58 C. Schmitz-Antoniak, D. Schmitz, A. Warland, M. Darbandi, S. Haldar, S. Bhandary, B. Sanyal and O. Eriksson and HW, Suppression of the Verwey Transition by Charge Trapping, *Ann. Phys.*, 2018, **530**(3), 1700363, DOI: 10.1002/andp.201700363.

59 J. H. Chen, W. J. Mi, H. Y. Chen, B. Li, K. C. Chou and X. M. Hou, Iron oxide recovery from fayalite in water vapor at high temperature, *J. Min. Metall., Sect. B*, 2018, **54**(1), 1–8, DOI: 10.2298/JMMB160926011C.

60 X. Li and J. Paier, Partial Oxidation of Methanol on the Fe3O4 (111) Surface Studied by Density Functional Theory, *J. Phys. Chem. C*, 2019, **123**(13), 8429–8438, DOI: 10.1021/acs.jpcc.8b10557.

61 S. R. J. Saunders, M. Monteiro and F. Rizzo, The oxidation behaviour of metals and alloys at high temperatures in atmospheres containing water vapour: A review, *Prog. Mater. Sci.*, 2008, **53**(5), 775–837, DOI: 10.1016/j.pmatsci.2007.11.001.

62 L. Suber, P. Imperatori, A. Mari, *et al.*, Thermal hysteresis of Morin transition in hematite particles, *Phys. Chem. Chem. Phys.*, 2010, **12**(26), 6984–6989, DOI: 10.1039/b925371h.

63 C. Belviso, E. Agostinelli, S. Belviso, *et al.*, Synthesis of magnetic zeolite at low temperature using a waste material mixture: Fly ash and red mud, *Microporous Mesoporous Mater.*, 2015, **202**(C), 208–216, DOI: 10.1016/j.micromeso.2014.09.059.